



Originally published as:

Toy, V. G., Mitchell, T. M., Druiventak, A., Wirth, R. (2015): Crystallographic preferred orientations may develop in nanocrystalline materials on fault planes due to surface energy interactions. - *Geochemistry Geophysics Geosystems (G3)*, 16, 8, p. 2549-2563.

DOI: <http://doi.org/10.1002/2015GC005857>



RESEARCH ARTICLE

10.1002/2015GC005857

Crystallographic preferred orientations may develop in nanocrystalline materials on fault planes due to surface energy interactions

Virginia G. Toy¹, Thomas M. Mitchell², Anthony Druiventak³, and Richard Wirth⁴

¹Department of Geology, University of Otago, Dunedin, New Zealand, ²Department of Earth Sciences, University College London, London, UK, ³Experimental Geophysics Laboratory, Institute for Geology, Mineralogy, and Geophysics, Ruhr-University Bochum, Bochum, Germany, ⁴GeoForschungs Zentrum Potsdam, Potsdam, Germany

Key Points:

- Silica nanopowder was generated on simulated faults in triaxial experiments
- Plastic basal plane defects are precursors to comminution to nanocrystals
- CPOs might result from surface energy interactions during nanopowder annealing

Correspondence to:

V. Toy,
virginia.toy@otago.ac.nz

Citation:

Toy, V. G., T. M. Mitchell, A. Druiventak, and R. Wirth (2015), Crystallographic preferred orientations may develop in nanocrystalline materials on fault planes due to surface energy interactions, *Geochem. Geophys. Geosyst.*, 16, 2549–2563, doi:10.1002/2015GC005857.

Received 13 APR 2015

Accepted 8 JUL 2015

Accepted article online 14 JUL 2015

Published online 14 AUG 2015

Abstract A layer of substantially noncrystalline material, composed of partially annealed nanopowder with local melt, was experimentally generated by comminution during ~ 1.5 mm total slip at $\sim 2.5 \times 10^{-6}$ m s⁻¹, $P_{\text{conf}} \sim 0.5$ GPa, and 450°C or 600°C, on saw cut surfaces in novaculite. The partially annealed nanopowder comprises angular grains mostly 5–200 nm diameter in a variably dense packing arrangement. A sharp transition from wall rock to partially annealed nanopowder illustrates that the nanopowder effectively localizes shear, consistent with generation of nanoparticles during initial fragmentation, not by progressive grain size reduction. Dislocation densities in nanopowder grains or immediate wall rock are not significantly high, but there are planar plastic defects spaced at 5–200 nm parallel to the host quartz grain's basal plane. We propose these plastic defects developed into through-going fractures to generate nanocrystals. The partially annealed nanopowder has a crystallographic preferred orientation (CPO) that we hypothesize developed due to surface energy interactions to maximize coincident site lattices (CSL) during annealing. This mechanism may also have generated CPOs recently described in micro/nanocrystalline calcite fault gouges.

1. Introduction

Recently, paradigms about the deformation mechanisms that can effectively accommodate seismic-rate slip in natural faults have been challenged by observations that microstructures characteristic of dislocation [e.g., Verberne *et al.*, 2013, 2014; Smith *et al.*, 2013] or diffusion creep [e.g., De Paola, 2013; Green *et al.* 2015; Schubnel *et al.*, 2013] can be generated on simulated fault planes sheared at seismic slip rates (i.e., >0.1 m s⁻¹) [Sibson, 1983] initially at room temperature conditions. It is generally inferred that short-lived dynamic frictional heat pulses and the ultrafine-grained nature of the fault rocks allowed these various sorts of creep to dominate. Calculations using reasonable flow laws seem to allow seismic strain rates to be accommodated by creep for very high stresses and fine particle sizes [e.g., Schubnel *et al.*, 2013], but the sensitivity to their chosen grain size yields orders of magnitude uncertainty to these estimates. Furthermore, frictional heat pulses are very short lived and it is difficult to understand how the observed microstructural changes could occur while this heating has a measurable effect.

Additionally, despite a growing number of careful studies correlating microstructural observations to slip rate behavior [e.g., Niemeijer and Spiers, 2005, 2006; Den Hartog and Spiers, 2013; Rowe *et al.*, 2011; Ikari *et al.*, 2011], there is still no firm consensus on what fine-grained fault rock microstructures are diagnostic of seismic versus aseismic faulting [Cowan, 1999; Stünitz *et al.*, 2010]. One category of fault rocks that have recently been “correlated” to seismic slip rate [Smith *et al.*, 2013] are amorphous and nanocrystalline materials [see, in particular, Kirkpatrick *et al.*, 2013]. Formation mechanisms and mechanical evolution of these materials potentially influence earthquake rupture nucleation and propagation, so they currently receive wide attention within the seismotectonic community [Reches and Lockner, 2010; Chen *et al.*, 2013].

In this study, we have generated nanocrystalline materials in simulated faults in very simple quartzites in a Griggs-type apparatus. We propose an explanation for their microstructures and textures that does not require deformation mechanisms more typically associated with aseismic creep. The observations we present, and our discussion of realistic mechanisms may allow greater confidence in interpretation of slip rate behavior from natural microstructures.

1.1. Amorphous and Nanocrystalline Materials on Fault Planes

The development of at least partially “amorphous” and/or “nanocrystalline” materials within fault principal slip zones has been shown to dramatically reduce their frictional shear resistance [Goldsby and Tullis, 2002], so it is proposed that the generation of these materials facilitates shear localization and seismic slip. Such microstructures have been generated experimentally in high-velocity ($< \sim 1 \text{ m s}^{-1}$) experiments with displacements ranging from 4 to 40 m conducted at room temperatures (e.g., silica gels reported by Di Toro *et al.* [2004]; granular nanomaterial described by Han *et al.* [2011]). They have also been observed in products of much lower velocity ($10\text{--}100 \mu\text{m s}^{-1}$) shear experiments at higher initial temperatures and confining pressures such as the apparent pseudotachylytes reported by Pec *et al.* [2012] that were generated at $T = 300^\circ\text{C}$, $P_{\text{conf}} = 500 \text{ MPa}$ in a Griggs-rig-type apparatus. Glassy/melt textures have also been shown to form on the surfaces of saw cut samples in standard triaxial deformation experiments conducted at axial strain rates of 10^{-4} s^{-1} [e.g., Friedman *et al.*, 1974] where localized high temperatures are reached due to rapid stick-slip events. Koizumi *et al.* [2004] showed that similar triaxial saw cut experiments at nominal axial strain rates of 10^{-3} s^{-1} demonstrate stick-slip events with peak velocities approaching 40 m s^{-1} over displacements of 0.32 mm at $P_{\text{conf}} = 150 \text{ GPa}$, and provided evidence of surface structures indicating that melt layers are formed as a consequence. More recently, Beeler *et al.* [2011] showed similar melt structures in Westerly granite formed during stick-slip events with peak velocities of $> 5 \text{ m s}^{-1}$ at $P_{\text{conf}} = 400 \text{ MPa}$. Amorphous materials have also been reported in natural fault zones (e.g., natural silica gel from the Corona Fault described by Kirkpatrick *et al.* [2013]). These materials commonly comprise some proportion of randomly oriented nanocrystals embedded in a noncrystalline matrix that displays no TEM diffraction contrast or lattice fringes. Proposed generation mechanisms include: irradiation damage, deformation, application of pressure, and chemical reactions; but reported microstructural observations are mostly consistent with micro/nanocomminution involving generation of lattice defects [Pec *et al.*, 2012, and references therein].

Recently, it has been found that some microcrystalline and nanocrystalline aggregates within the principal sliding surfaces of calcite and halite gouges deformed experimentally at coseismic or subseismic rates have developed crystallographic preferred orientations (CPOs) [e.g., Kim *et al.*, 2010; Verberne *et al.*, 2013]. In addition, Smith *et al.* [2013] presented microstructural evidence that such a granular material was annealed and subsequently dynamically recrystallized. A growing number of studies reveal CPOs can develop in materials experimentally deformed by diffusion-dominant processes [e.g., Sundberg and Cooper, 2008], or due to oriented growth in a strain field [e.g., Shelly, 1971]. Nevertheless, the simple observation that most tectonites with strong CPOs also have microstructures typical of dislocation creep (e.g., stretched grains, undulose extinction, interlobate grain boundaries) [Tullis *et al.*, 1973; Schmid and Casey, 1986; Law, 1990; Heilbronner and Tullis, 2006] dictates that the most important mechanism of CPO development in silicate minerals is dislocation glide, a component of “grain size insensitive” or “dislocation creep.”

CPOs and annealed textures were also reported in micron-sized quartz grain aggregates adjacent to pseudotachylytes described by Bestmann *et al.* [2011, 2012]. These potentially also developed due to grain size insensitive creep at enhanced rates due to thermal effects adjacent to the friction melts.

Grain size insensitive creep is the dominant strain-accommodating mechanism in solid-state flow of rock when homologous temperatures (i.e., T/T_m) exceed ~ 0.5 [Carter, 1976]. However, synthetic gouges within which CPOs were developed would have been subjected to such elevated temperatures for very short time periods. Smith *et al.* [2013] calculated the maximum temperature achieved within the $< 300 \mu\text{m}$ thick calcite gouge layers in their high-velocity (1 m s^{-1}) experiments as 900°C . Thermal diffusion from an infinite tabular zone of this thickness and uniform starting temperature into host rock at room temperature (at which their experiments were performed) would result in cooling of the entire material below 50°C in $< 3 \text{ s}$ (full calculations in Appendix A).

Rates of dynamic recrystallization are very difficult to quantify, but at rates of grain boundary migration calculated by Prior *et al.* [1990] in New Zealand's Alpine Fault mylonites subject to simple shear at 10^{-10} s^{-1} and temperatures in the range $350\text{--}600^\circ\text{C}$, a grain boundary requires 26 years to migrate through a $1 \mu\text{m}$ diameter grain (260 years for a $10 \mu\text{m}$ grain). There is no straightforward way to extrapolate this calculation to experimental conditions, but we anticipate greater driving forces due to the much higher experimental strain rates in the calcite gouges would have been offset by reduction in boundary migration rates at the low temperatures. Thus, it is difficult to understand how dynamic recrystallization could have occurred in the available time.

We note that cellular nanograins have been formed in experiments on metals by a combination of microfracture and subgrain wall formation (i.e., dislocation glide and recovery) at room temperature and strain rates comparable to those realized in *Verberne et al.*'s [2013] nanocrystalline calcite gouge experiments [Umamoto, 2003; Yang et al., 2010]. However, metals generally have melting, and therefore homologous temperatures less than half those of silicate minerals [Haynes, 2014], so we do not anticipate this process is anywhere near as effective in the latter.

At present, we believe that a conclusion that CPOs in both materials mostly result from operation of dislocation processes requires dramatic revision of paradigms about the likely rates of microstructural change in deforming rock. Herein we propose an alternative explanation for the observed CPOs, involving surface energy interactions during annealing and examine this in context of our own experimental data.

2. Experimental Setup and Results

Typical seismic slip rates (meters per second) [Sibson, 1983] cannot yet be achieved in experimental apparatus' at confining pressures and temperatures characteristic of the base of the seismogenic zone, which is the nucleation region of large earthquakes. Consequently, we have simulated accelerated creep shear beneath the interseismic "brittle-ductile transition," as would occur during downward propagation of earthquake ruptures nucleated in the brittle field. These simulated earthquakes were induced in a Griggs-type apparatus [Rybacki et al., 1998; Griggs, 1967] at Ruhr-Universität Bochum, Germany. A single saw cut was made at 45° to the long axes of 3.3 mm diameter and 7.01 mm long cylinders of Arkansas novaculite (donated to Prof. J. Renner of Ruhr-Universität Bochum by Dr. C. Stone, Geological Survey of Arkansas) [Keller et al., 1985]. The specimens were jacketed in gold capsules, and NaCl served as a confining medium (similar to experiments at 300°C and 600°C described by *Druiventak et al.* [2011]). They were heated to 450°C (sample RUB-1) and 600°C (sample RUB-2) under 0.50 GPa (2 s.f.) confining pressure, at $\sim 0.08^\circ\text{C s}^{-1}$. Axial loads were then applied until shear occurred on the simulated fault surface.

Slip rates of $2.5 \times 10^{-6} \text{ m s}^{-1}$ (2 s.f.) allowed total slip, \bar{u} , of 1.5 mm (2 s.f.) parallel to the cut surface to be achieved in 10 min. Total slip, initially determined from displacement of the axial pistons, was confirmed by measuring the samples once they were removed from their jackets and cut in half (e.g., insets in Figure 1). Failure and stable sliding occurred at peak differential stresses of 0.42 GPa (2 s.f.) and 0.35 GPa (2 s.f.) respectively, followed by significant weakening (Figure 1). During ongoing shear, there were small rapid fluctuations in the stress-displacement curve that appear to increase in frequency around the peak stress and continue throughout the sliding. These variations may be discrete "stick-slip" events, but could also be boundary artifacts due to the complex jacketing arrangement in a Griggs-type apparatus. The samples were left to cool overnight (~ 16 h) before removal from the apparatus.

3. Microstructural Observations

Microstructures of the novaculite within and surrounding the simulated fault surface, and of the material generated on the simulated fault, were examined using standard optical microscopy at the University of Otago. Secondary and backscatter electron images and crystallographic orientation measurements were also obtained using a LEO (Zeiss) 1530 Gemini FE-SEM with an Oxford Aztec HKL EBSD system housed at Ruhr-Universität Bochum and a Zeiss Sigma VP FE-SEM with an HKL INCA Premium Synergy Integrated ED/EBSD system housed at the University of Otago. All observations were made in thin sections cut parallel to the shear direction and the cylinder long axes; TEM (150 nm thick) foils were milled from these sections normal to the surface of the thin section using the focused ion beam FEI FIB200 instrument operating at GeoForschungs Zentrum GFZ Potsdam. For details of this FIB milling, see *Wirth* [2004]. Transmission electron microscopy (TEM) was performed in a FEI G2 F20 X-Twin electron microscope with a Schottky field emitter as electron source. The TEM is equipped with a Gatan Tridiem™ imaging filter, a Fishione high-angle annular darkfield (HAADF) detector, and an EDAX X-Ray analyzer. Brightfield and darkfield images usually were acquired as electron filtered images applying a 20 eV window to the zero-loss peak. Electron diffraction patterns were recorded on image plates.

3.1. Host Rock

Undeformed novaculite furthest from the simulated fault plane is 99% quartz + a brownish, unidentified phyllosilicate mineral. The quartz grains are 5–15 μm in diameter, fairly equant, lack a preferred orientation,

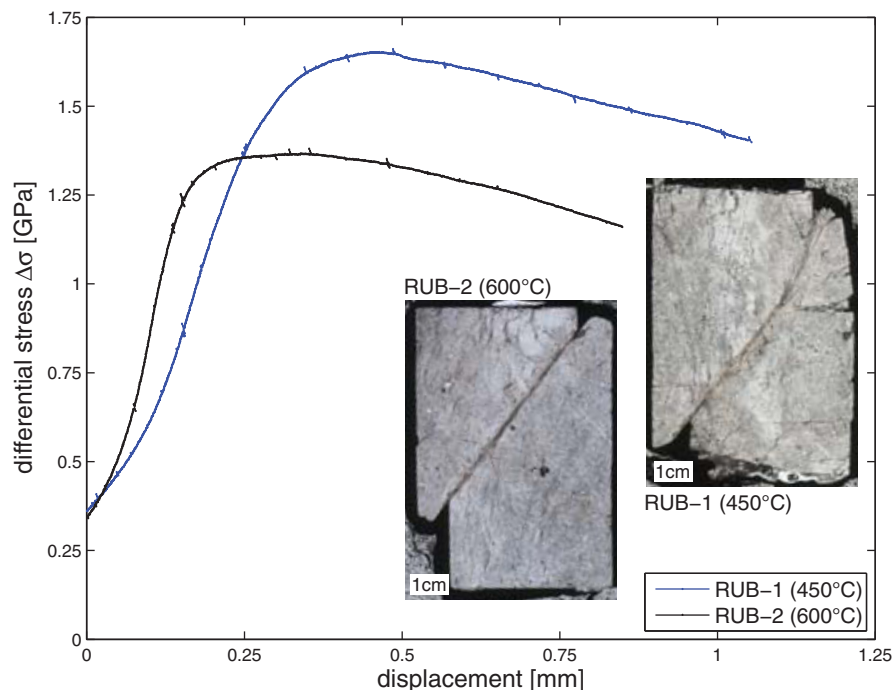


Figure 1. Differential stress versus displacement of the axial pistons during the experiments. Slip on the simulated fault is 1.4X the displacement indicated here since the saw cut surfaces are inclined at 45° to the cylinder long axis. Insets are scans of sample thin sections cut parallel to slip direction and cylinder long axes.

and are divided by organized high-angle grain boundaries (Figures 2a–2c). The grains contain disordered groups of primary fluid inclusions (i.e., having formed during precipitation of the quartz grain) (Figure 2d) as well as planar arrays of stretched fluid inclusions decorating healed microfractures (“planar deformation features” of *Blenkinsop* [2000]; Figure 2e) and rare microfractures. The grains are mostly dislocation free but scattered loop-shaped dislocations are locally observed, particularly around impurities such as fluid inclusions and grain boundaries (Figure 2e), and very rarely, these dislocations are weakly aligned into planar arrangements (Figure 2f).

3.2. Material Adjacent to the Saw Cut Surface (Wall Rock)

Most grain boundaries adjacent to the simulated fault are dilated by at least 0.1 μm but in some cases up to 50–150 μm . Elsewhere within the host novaculite only a small proportion of grain boundaries are similarly open. Dislocation densities are not notably higher in the immediate wall rock of the simulated fault than elsewhere in the samples.

The most prominent feature within wall rock in both samples are planar defects in the crystal structure of ~ 5 nm width spaced at 5–200 nm that truncate or interrupt diffraction contrast bands but do not necessarily displace these bands laterally (Figures 3a and 3b). The features are not commonly associated with dislocations, although in places there are moderately elongate patches of the material containing arrays of disordered dislocations that are parallel to the planar defects. HR-TEM imaging reveals the planar defects comprise a slight disordering of the long-range structure of the host grain (Figure 3c). Diffraction spot spacing (Figure 3d) is compatible with them being parallel to the basal (0001) plane of the host grain.

3.3. Material Within the Slip Zone

In both RUB-1 and RUB-2, a layer of noncrystalline silica was developed on the saw cut surface during deformation (Figure 4). This layer is 50–100 μm thick in RUB-1, 20–50 μm thick in RUB-2, and translucent with a brownish tint. It contains hairline darker seams that delineate pods of the material with long axes inclined with the sense of shear at $\sim 25^\circ$ to the shear plane. It is mostly isotropic, but in places, a slight foliation that is similarly oblique to the shear plane is indicated by a uniform extinction angle (appearing similar to a colorless phyllosilicates; Figures 4a and 4b). The layer boundaries are not entirely planar; deflections are

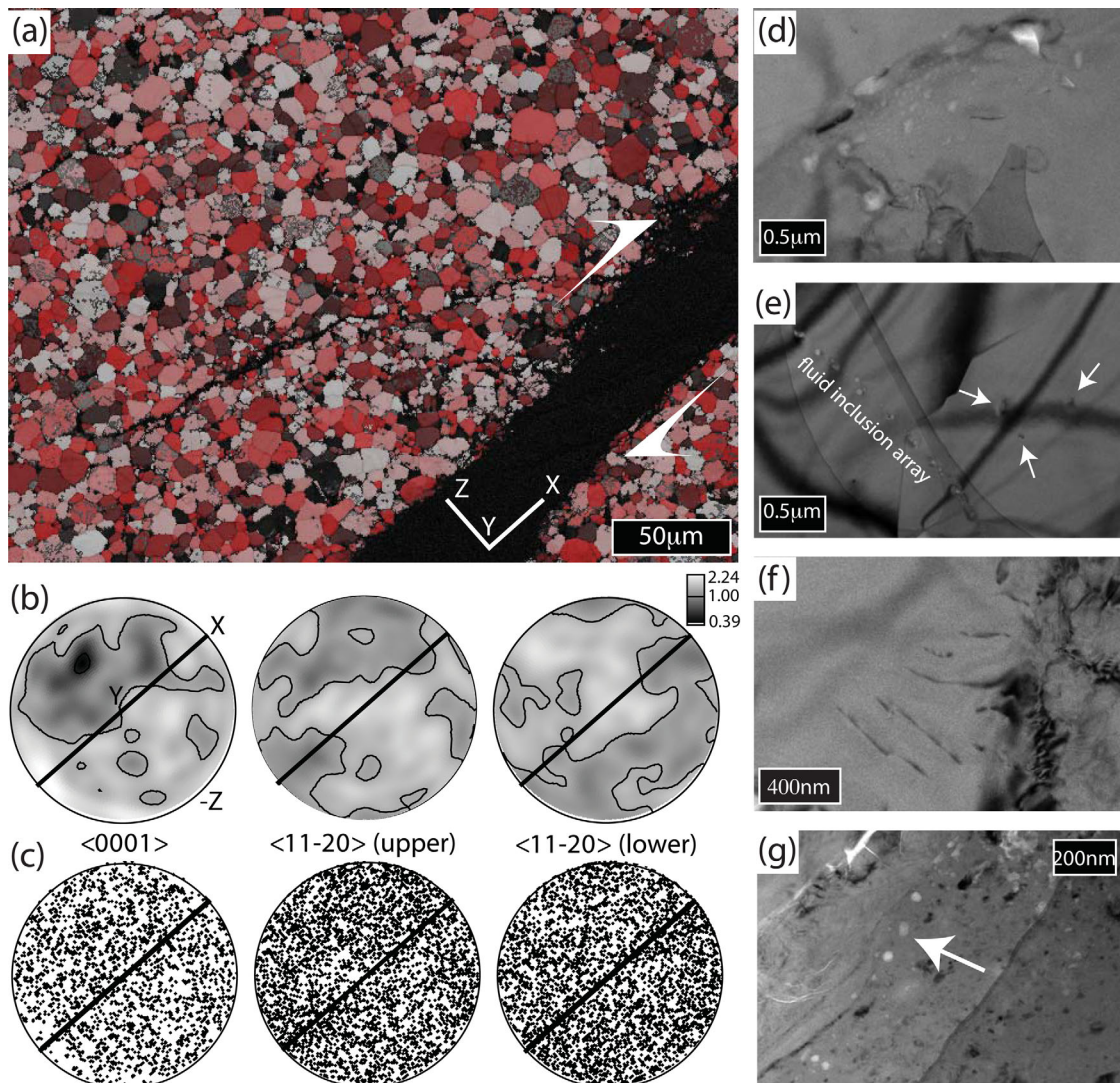


Figure 2. (a) EBSD-derived map of an area of RUB-1 including the simulated fault. Color scheme indicates Schmid Factor (i.e., stress on that slip system as a fraction of the maximum possible shear stress) for the basal $\langle a \rangle$ slip system in quartz, with load parallel to the sample long axis which is horizontal in this image. Arrows indicate shear sense on simulated fault. (b) Contoured, and (c) point distributions of $\langle c \rangle$ and $\langle a \rangle$ crystallographic axes of quartz on lower hemisphere, equal area projections. Kinematic reference frame is as indicated in Figure 2a; $n = 3605$; 1 point per grain; only grains $> 1.5 \mu\text{m}$ diameter are plotted; contour scale is in multiples of uniform density. Brightfield TEM images of (d) disordered group of fluid inclusions (RUB-1); (e) planar array of stretched fluid inclusions (RUB-1). Scattered dislocations are present—indicated by white arrows; (f) array of dislocations around a grain boundary, weakly aligned into a planar arrangement (RUB-2). (g) Noncrystalline material in RUB-1 containing rounded low-density areas inferred to be bubbles (arrowed).

particularly associated with fractures that splay off the main fault plane but do not appear to have accommodated significant shear displacement. At one end of the sheared zone in RUB-1, the single zone diverges into a series of subparallel splay faults bounding slivers of the host rock dissected by regular fractures at high angles to the bounding faults. The transition from the foliated material to the wall rock is mostly sharp but locally there are pods and zones of cataclaste comprising partially fragmented host rock.

On insertion of a full lambda retardation plate, the apparently noncrystalline material displays evidence of a preferred crystallographic alignment, turning more red/yellow or more blue/purple at certain rotations of the stage with respect to the polarizers and retardation plate. This alignment must be contained within crystalline fragments within the aggregate. Since the material is silica, crystalline fragments will be quartz, and we can infer the optically slow direction, which is parallel to the c axis, dominantly subtends an angle of 54° to the main shear plane, and is inclined in the sense of shear (Figures 4c and 4d).

Most of the noncrystalline material within the simulated fault plane displays no TEM individual diffraction contrast and cannot be indexed using EBSD (Figure 2a), even with the high precision offered by FE-SEM. It

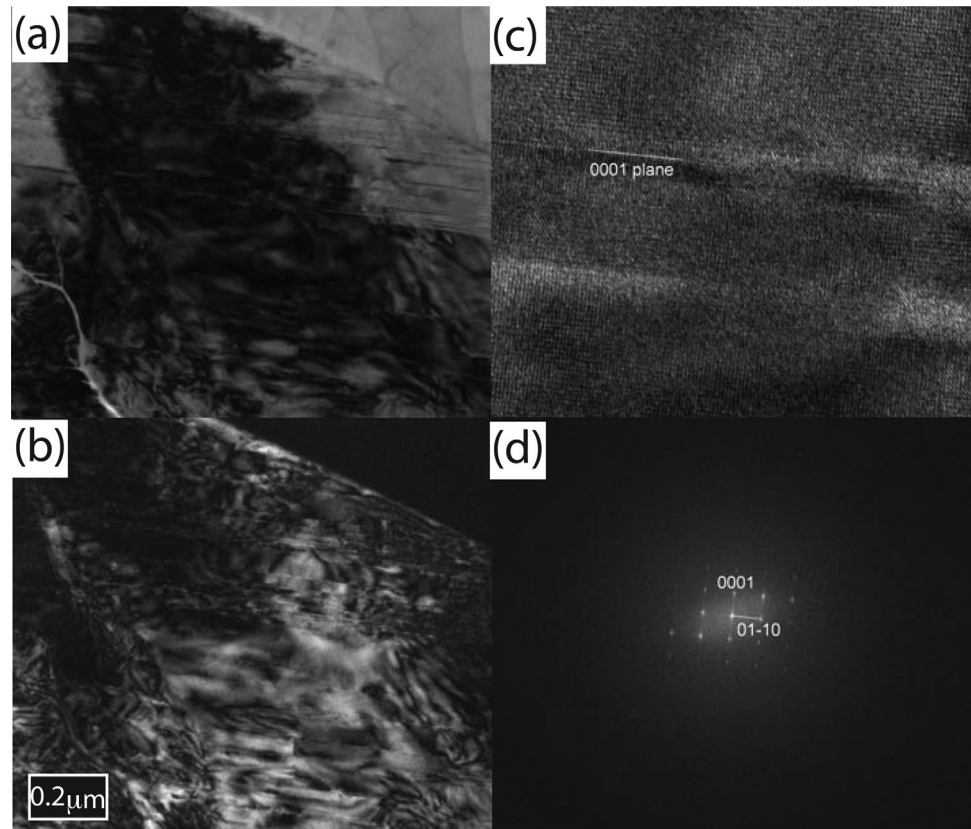


Figure 3. TEM images from RUB-1 of closely spaced planar features in (a) bright field, (b) dark field, (c) HR-TEM, and (d) illustrating an indexed diffraction pattern obtained via FFT of HR-TEM. All planar features are parallel to the basal (i.e., (0001)) plane of the host quartz grain, and within them the long range order of the crystal lattice is slightly disturbed.

is mostly a uniform grey shade, consistent with lack of crystalline structure, but in brightfield TEM images, it sometimes has patches of varying brightness—the brighter patches are overall thinner so show less mass absorption of the primary electrons. Some of these have rounded shapes suggesting that they are bubbles (Figure 2g). There are also darker or brighter subangular to subrounded patches measurably from 5 to 200 nm in diameter, which are fragments of crystalline material. Some display moiré patterns indicating that they are thinner than the foil thickness (~150 nm) and overlie other fragments of crystalline material. There is no evidence of high dislocation densities within these crystalline fragments. The percentage of these crystalline fragments decreases but they become larger toward the centers of the mostly noncrystalline zones.

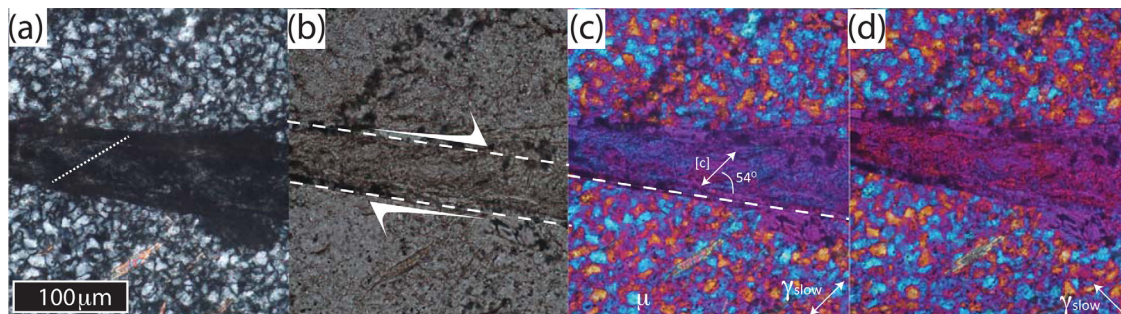


Figure 4. Photomicrographs of sheared zone and immediate wall rock in RUB-1. (a) Crossed polars; dotted white line indicates a preferred alignment of extinction angle; i.e., of grains. (b) Same area in plane polarized light. White dashed lines indicate the shear plane and arrows the shear sense. (c and d) Also the same area with the gamma plate inserted in the orientation annotated at lower right of the images. Variation from blue to orange colors within the nanopowder with 90° rotation of the plate results from changes in relative retardation of transmitted light, indicating the presence of a CPO. If these grains are quartz, the color changes observed here suggest [c] trends top right-bottom left of the zone as annotated in Figure 4c.

TEM-scale structure of the noncrystalline material is exemplified by our foil #3217, which was cut across the transition from damaged wall rock through gouge and into the noncrystalline material in RUB-1 (Figure 5a). The foil contains a zone of intact quartz host rock grains $>8 \mu\text{m}$ thick at left of this figure. In the center, there is a $4 \mu\text{m}$ thick layer of angular, elongate fragments of quartz smaller than the parent grain size, with a weak foliation defined by the long axes of the fragments. At right of the foil, there is a layer $3 \mu\text{m}$ thick (entire layer is not included in foil so this is a minimum thickness) of mostly grey (i.e., no diffraction contrast so noncrystalline) material with rare light and dark patches that contain diffraction contrast bands indicating they are crystalline. These crystalline fragments are subangular and $5\text{--}200 \text{ nm}$ in diameter, thus are correctly named "nanocrystals." They might be an assembly of nanocrystals with almost the same orientation thus forming a kind of mosaic crystal, which is indicated by slight changes in contrast. The transition between the layer of quartz fragments and the mostly noncrystalline layer is reasonably sharp. Both layers have very variable grey shades, suggesting variable density, but the variations are more pronounced in the cataclasite than in the noncrystalline material. Electron diffraction patterns were obtained from the mostly noncrystalline layer and the layer of quartz fragments (Figures 5b–5e). The diffraction pattern from the noncrystalline layer shows some diffuse scattering intensity but also pronounced Debye-Scherrer rings with some preferred orientations (i.e., concentrations of high scattering intensity in particular positions within the rings). The cataclasite yields a similar diffraction pattern, but the strong scattering intensities within the Debye-Scherrer rings are more smeared out along particular rings, indicating fewer systematic crystal orientations within this material. The Debye-Scherrer rings in the noncrystalline layer show strong concentrations at inclinations to the shear plane of $45\text{--}70^\circ$, $128\text{--}145^\circ$ (outer ring; which is indexed (10–11)), and $80\text{--}95^\circ$ (inner ring; which is indexed (01–10); Figure 5e). The concentrations in the outer ring are therefore $\langle a \rangle$ axes or poles to prism planes (m-planes), while the concentrations in the inner ring are c axes or poles to basal planes. Conversely, optical petrography suggests a c axis inclined at 54° to the shear plane (Figure 4). However, the angle at which the material displays maximum or minimum retardation of transmitted light when the gamma plate is inserted is slightly different in patches throughout the layer, and the TEM foil was not extracted from the same thin sections as are available for optical studies, so we cannot confirm the exact orientation relationships. We suspect that the orientations observed in the foil are only applicable at that location.

4. Discussion

4.1. Origin of the Mostly Noncrystalline Material

The formation mechanisms that have been previously inferred for nanocrystalline or amorphous materials on natural or simulated (geological) fault surfaces are melting, tribochemical reactions, and micro/nanocomminution [e.g., Han et al., 2011; Kirkpatrick et al., 2013; Pec et al., 2012; Sibson and Toy, 2006].

4.1.1. Melting

A local temperature increase should have been concentrated around the simulated fault due to frictional heating. Lee and Delaney [1987] proposed the temperature rise, δT , due to frictional heating induced by shear on a frictional interface, which can be approximated by:

$$\delta T = \frac{\bar{u}\tau}{\rho c \sqrt{\frac{\pi}{4\kappa ts}}} \quad (1)$$

so for realistic values of average slip, $\bar{u} = 1.5 \text{ mm}$; shear stress, $\tau = \Delta\sigma_{\text{max}}/2 = (0.42 \times 10^9)/2 \text{ Pa} = 2.8 \times 10^8 \text{ Pa}$; specific heat capacity, $c = 1200 \text{ J kg}^{-1} \text{ }^\circ\text{C}^{-1}$; host rock density, $\rho = 2700 \text{ kg m}^{-3}$; thermal diffusivity, $\kappa = 1 \times 10^{-6} \text{ m}^2 \text{ s}^{-1}$; duration of slip, $ts = 600 \text{ s}$, we find that the temperature rise on the simulated fault during both experiments could have been 4.7°C (2 s.f.). A melt origin for the entire noncrystalline layer can therefore be discounted because this bulk temperature increase is insufficient to melt the novaculite (T_{melt} of pure quartz is $\sim 1270^\circ\text{C}$; and $\sim 1100^\circ\text{C}$ for hydrous conditions) [Hall, 1996; Boullier et al., 2001, and references therein].

However, if stick-slip events occurred during the experiment [Friedman et al., 1974; Koizumi et al., 2004], significantly higher slip rates should have occurred for very short time periods, during which frictional heat would not diffuse off a single shearing surface. In this case, during $100 \mu\text{m}$ shear displacement, a melt layer $\sim 8.5 \mu\text{m}$ thick could be generated (full calculations in Appendix B). Local generation of melt within our experiments would neatly explain bubbles locally observed in the noncrystalline layer decorating the simulated fault. However, heat would have diffused away from the slip zone over the entire experiment duration,

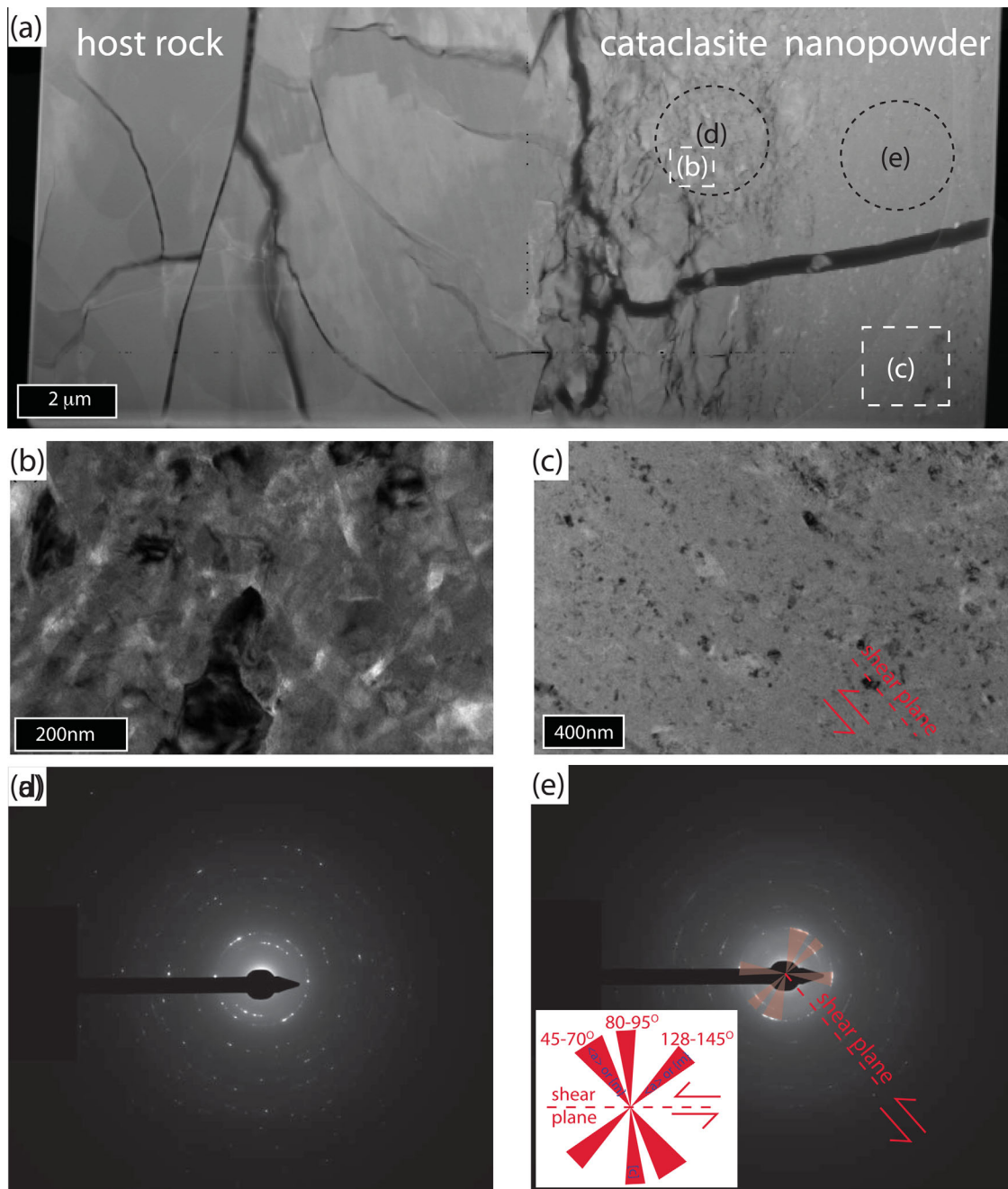


Figure 5. TEM images illustrating (a) high-angle annular darkfield image (HAADF) overview of foil #3217 illustrating zones (from left to right) of host rock, cataclasite, and partially annealed nanopowder. Boxes and ellipses indicate areas enlarged/sampled in Figures 5b–5e. (b and c) TEM brightfield images: appearance of cataclasite and partially annealed nanopowder; electron diffraction patterns from (d) cataclasite and (e) partially annealed nanopowder illustrating more systematic orientations (bright streaks in Debye-Scherrer rings) in the latter. Note the higher diffuse scattering intensity due to the presence of noncrystalline material or nanocrystalline grains (<10 nm) in Figure 5e. The inset in Figure 5e illustrates orientations and possible interpretations of the crystallographic axes from indexing of the diffraction spots that display concentrations within the Debye-Scherrer rings.

and we would expect noncrystalline material with a melt origin to have fairly uniform density, which is inconsistent with most of our microstructural observations. Thus, we do not believe the entire layer was generated by melting.

4.1.2. Tribochemical Reactions

On the surface of a silicate, atoms are not in their ideal geometric arrangement [Iler, 1979] and have high elastic strain energies [Gleiter, 1989]. Consequently, tribochemical reactions (reactions between surfaces and lubricants as they shear against one another) [Hsu *et al.*, 2002] that reduce these elastic strains, presumably by reconstructing an intact lattice, are energetically favored on surfaces. In nanomaterials, which have

particularly large areal ratios of surface:particle interior [Gleiter, 1989] such as existing fragmented materials, these reactions are particularly favored. However, they cannot be the driving mechanism of production of amorphous materials in the absence of another mechanism of production of new surfaces; they can only contribute to formation of further subcrystalline material as experiments (or natural seismic slips) progress.

4.1.3. Micro/Nanocomminution

The angular nature of the crystal fragments and variable density of the noncrystalline material (Figure 5c) strongly support the hypothesis of generation by a cataclastic process. The variable density reflects variable compaction of a granular aggregate, so it is logical that density variations are greatest in the cataclasite and less apparent in the noncrystalline material. The noncrystalline material therefore originated as a *variably dense nanopowder*. This nanopowder seems to have been more “well developed” (it is a thicker layer, with fewer nanocrystalline fragments) in the lower-temperature experiment, as we could expect if it forms by brittle failure.

Comminutive processes are thought to be unfavorable at this fine scale. It has previously been proposed [Keulen *et al.*, 2008] that 1 μm is the “grinding limit” for quartz; beneath this size, the stresses and stressing rates required to generate transgranular fractures are higher than can realistically be generated by particle-on-particle impacts and grains tend to deform plastically rather than fracturing [Kendall, 1978]. Thus, it is difficult to understand how the nanocrystalline fragments were generated by cataclasis. Furthermore, the partially annealed nanopowder layer continues all the way to the sample ends, where only very small increments of shear occurred between the “wall rocks,” and there is no transitional zone of gradually increasing grain size into the wall rock. These observations suggest that this layer of very fine particles is generated early during shearing and that once it is present, strain is very effectively localized into it. The absence of higher-than-background dislocation densities in the immediate wall rock to the simulated fault, in the cataclasite fragments, or in clasts in the gouge, suggests that comminution does not follow from generation of excessive dislocation densities and organization of these into subgrains as described by Yang *et al.* [2010]. Instead, we infer that the fragmentation occurred mostly by generation of, and eventual complete failure along, the planar defects we have described that are parallel to the basal plane of the host quartz grains. Comparable features are commonly described in quartz that has been subject to transiently high stresses during shock loading such as around meteor impact structures [e.g., Trepmann, 2008]. This process would generate grains ranging from 5 to 200 nm in diameter and a significant proportion of the resultant nanoparticle boundaries would be preferentially parallel to the basal plane. Finer, noncrystalline particles may also be generated during breakdown of the material within the planar defects. This hypothesis requires more rigorous experimental investigation than has been possible during the current study and will be subject to future investigation.

4.2. CPO Development Due to Surface Energy Interactions During Annealing

Partially annealed nanopowders like we describe comprise aggregates with some proportion of small (5–200 nm) angular cores of crystalline materials and surrounding amorphous material [Gleiter, 1989, 2000; Han *et al.*, 2011]. The ratio of grain surfaces, which have amorphous structure, to grain interior in these materials is very high (>50%), so the material has amorphous properties to most standard methods of structural investigation (e.g., XRD, TEM diffraction) [Gleiter, 1989, 2000]. Because of this high proportion of surface:crystal, surface interactions are likely to be very important in the materials’ evolution.

It has been demonstrated that surface energy anisotropy can result in rotation of particles into preferred alignments that maximize the number of shared lattice sites between the bounding grains (i.e., coincident site lattices, CSL) [Kronberg and Wilson, 1949] during annealing [e.g., Chan and Balluffi, 1985]. This process also affects airborne smoke particles of MgO and CdO generated by burning [e.g., Mykura *et al.*, 1980]. Chaudhari and Matthews [1971] observed that the number of smoke particles aligned to maximize CSL increases with increasing temperature. The material we describe from the simulated fault plane is cohesive, thus we infer that some amount of annealing affected the nanopowder grains after their formation by comminution, resulting in formation of intact interparticle boundaries. Microstructural observations in the calcite gouges with CPOs also reveal many cohesive grain boundaries [Smith *et al.*, 2013]. Particle rotations occur during annealing even at $T/T_m \sim 0.5$ [Chan and Balluffi, 1985], the lower limit at which grain size sensitive creep accommodates strain more easily than brittle processes [Carter, 1976]. We hypothesize that the CPOs in our quartzose partially annealed nanopowder, and in the calcite gouges described by others, developed

due to rotation of nanoparticles to maximize CSL and thus minimize surface energy during an annealing process.

In the bulk nanopowder, [c] subtend an angle of 54° to the shear plane as previously noted (Figure 4), while locally within the gouge (Figure 5), [c] subtend angles of $80\text{--}95^\circ$ and $\langle a \rangle$ are aligned in two groups, at $45\text{--}70^\circ$ and $128\text{--}145^\circ$. The angles between these $\langle a \rangle$ axis groups range from 58 to 100° . In intact quartz crystals, we would generally expect $\langle a \rangle$ axes to subtend angles of 60° (or multiples thereof) to one another. The fact that they do not do so in the partially sintered nanopowder strongly suggests that another process influences their alignment, as considered further below.

4.2.1. Preferential Alignment of Crystallographically Systematic Surface Orientations to the Shear Plane

In quartz, generation of nanocrystals by failure on plastic defects such as we describe, that are parallel to the basal plane of quartz, would impose such crystallographically systematic surface orientations. Natural quartz may also fracture preferentially parallel to $z\{01\text{--}11\}$ and $m\{10\text{--}10\}$ planes [Borg, 1956; Hearmon, 1956]. There may also be fragments generated by breakdown of the silica lattice within the planar defects, which will be noncrystalline and therefore cannot have crystallographically systematic surface orientations. In calcite, fragmentation also exploits crystallographically controlled twin planes and cleavages, so many fragment surfaces should also have crystallographically systematic surface orientations.

These surfaces might rotate with shear until parallel to the shear plane, which is a fabric attractor [Passchier, 1997], or at 45° to the shear plane, which is the plane of maximum instantaneous shear strain rate and therefore of maximum resolved shear stress, τ_{\max} , in simple shear [Ramsay, 1980; Simpson and De Paor, 1993]. This would result in angular relationships of [c] to the shear plane of 0° , $\sim 45^\circ$, and $\sim 90^\circ$ (Table C1), the latter two of which are broadly consistent with the orientations we observe.

4.2.2. Formation of CSL Boundaries During Sintering

First, note that there is no particular reason that intact boundaries should have a predictable geometric relationship to a shear plane. However, if CSL boundaries form in systematic orientations with respect to crystallographically systematic surface orientations, then a CPO may form in the bulk aggregate.

McLaren [1986] analyzed possible CSL in quartz, both for boundaries that exploit known twin planes, and for other possible boundary orientations with respect to the crystal lattice. He found that the most favored CSL, i.e., those that maximize the fraction of coincident lattice points, in order of preference are the Breithaupt, Sardinian, Cornish, and Japan twins and a particular nontwin plane. As described in Appendix C, we rotated a quartz crystal structure according to the angular relationships of these twin boundaries, and determined the possible angles between $\langle a \rangle$ axes. These angular relationships were then compared to those observed in the nanopowder.

From this comparison, we conclude that some of the observed $\langle a \rangle$ axis orientations in the nanopowder are consistent with CSL orientations only if one of the $\langle a \rangle$ axes aligns to the shear plane (Figures C1d and C1e). However, the predicted and observed interaxis angles are not perfectly coincident (e.g., $\langle a \rangle$ axes aligned at angles of $75\text{--}85^\circ$ or $95\text{--}105^\circ$ to the shear plane are predicted by this analysis, but not observed). It may be that a diffraction pattern from another site in the nanopowder would yield a different relationship. Alternatively, it may be that some of the theoretically favored CSL do not actually form in the real case. What is reassuring is that the analysis predicts that most $\langle a \rangle$ axes should align at angles greater than 60° to the shear plane, and we also do not observe a significant proportion of angles between 0° and 60° in the natural case.

4.2.3. Observation of Orientation Relationships of Individual Boundaries in the Sintered Nanopowder

To unequivocally validate our hypothesis, we would need to examine the crystallography and structure of newly formed grain boundaries in partially annealed nanopowders. Unfortunately, this is not possible in the quartz aggregates we describe, as the grain size is smaller than the typical activation volume for electron diffraction studies [Prior et al., 1990]. The emerging transmission kikuchi diffraction technique (TKD) [Trimby, 2012] might allow such data to be obtained, but is more likely to be successful in aggregates of silicate minerals (e.g., olivine, anorthite, calcite) other than quartz, which is very susceptible to electron beam damage. We aim to undertake such studies in the near future.

Verberne et al. [2013] noted the possibility that particle rotation during annealing imposes a CPO, and the idea was further developed by Verberne et al. [2014], who presented TEM evidence that annealed particle

boundaries exploit an expected CSL orientation in calcite, which strongly supports our hypothesis. Unfortunately, it is not possible to measure the orientation relationships between individual grains from our material due to the beam-sensitive nature of quartz.

4.2.4. Broader Implications

Both *Bestmann et al.* [2011, 2012] and *Pec et al.* [2012] described comparable natural and experimental faults in quartzite. However, there are notable differences in grain sizes, dislocation densities, and CPOs in the microstructures that developed in our experiments and those they describe. Furthermore, we do not observe a significant volume of solidified friction melt. We suggest this reflects that significantly more slip was accommodated on the faults these authors describe than was imposed in our experiments. Our observations are relevant to the processes that occur during rupture initiation, rather than after significant shear displacement has occurred.

It is interesting to consider (1) whether surface energy interactions are important without annealing and (2) what the long-term evolution of strength in a material subject to such surface energy interactions would be.

5. Conclusions

A noncrystalline material containing low densities of subangular nanoparticles, best described as a “variably dense and partially annealed nanopowder,” was generated at slip rates of rates of $\sim 2.5 \times 10^{-6} \text{ m s}^{-1}$ to total displacements of $\sim 1.5 \text{ mm}$ on a simulated fault plane in novaculite (i.e., quartzite). The most likely generation mechanism is comminution, wherein the “grinding limit” of quartz was overcome by plastic(?) generation of closely spaced lattice defects parallel to the basal plane. Melting may also have occurred locally during accelerated “stick-slip” events. Once present, shear was very effectively localized into this material. The material has a crystallographic preferred orientation (CPO) that we hypothesize was generated due to surface energy interactions to maximize coincident site lattices (CSL) and thus minimize surface energies. This mechanism is likely to have also been important in generation of CPOs recently described in other micro/nanocrystalline fault gouges, so extremely rapid rates of crystal plastic processes need not be invoked to explain their generation.

Appendix A: Cooling of a Gouge Layer

The temperature distribution in and around the gouge layer was modeled using the approximation for cooling of a thin, infinite sheet by conduction perpendicular to its margins presented by *Stüwe* [2002], wherein the temperature, T , at any point is given by:

$$T = T_i + \left(\frac{T_g - T_i}{2} \right) \left[\operatorname{erf} \left(\frac{0.5l - z}{\sqrt{4\kappa t}} \right) + \operatorname{erf} \left(\frac{0.5l + z}{\sqrt{4\kappa t}} \right) \right]$$

where:

- l the half thickness of the gouge layer;
- T_g initial temperature of the gouge layer;
- T_i the initial host rock temperature;
- K thermal diffusivity of both gouge and host rock, taken as $10^{-6} \text{ m}^2 \text{ s}^{-1}$;
- z distance from the center of the gouge layer;
- t time (s).

Results are illustrated in Figure A1.

Appendix B: Melt Layer Thickness

Following *Di Toro et al.* [2005], we calculate the thickness, t_m , of a layer of melt generated due to frictional heating on any sliding surface assuming no heat diffusion according to:

$$t_m = \frac{\tau_f \bar{u}}{\rho_{rock} (c_p \Delta T + \Delta h_{fus} (1 - \phi))} \tag{B1}$$

where

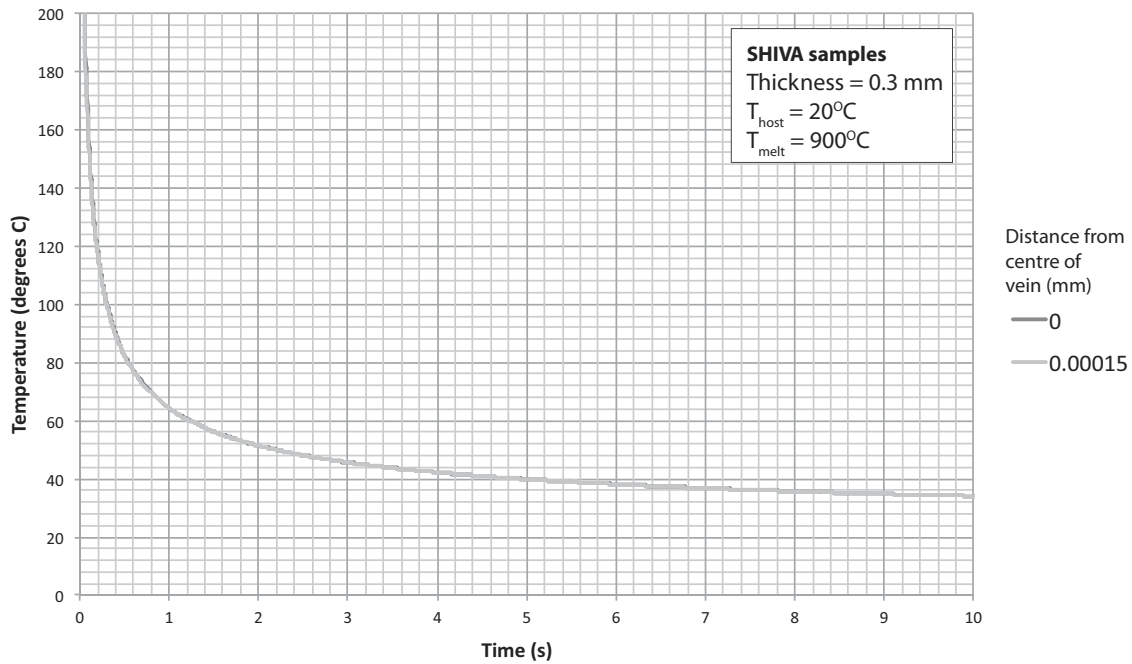


Figure A1. Temperature distribution during cooling at center (0 m) and margin (0.00015 m) of 300 μm thick calcite gouge layer heated to 900°C, in a host rock at room temperature (20°C).

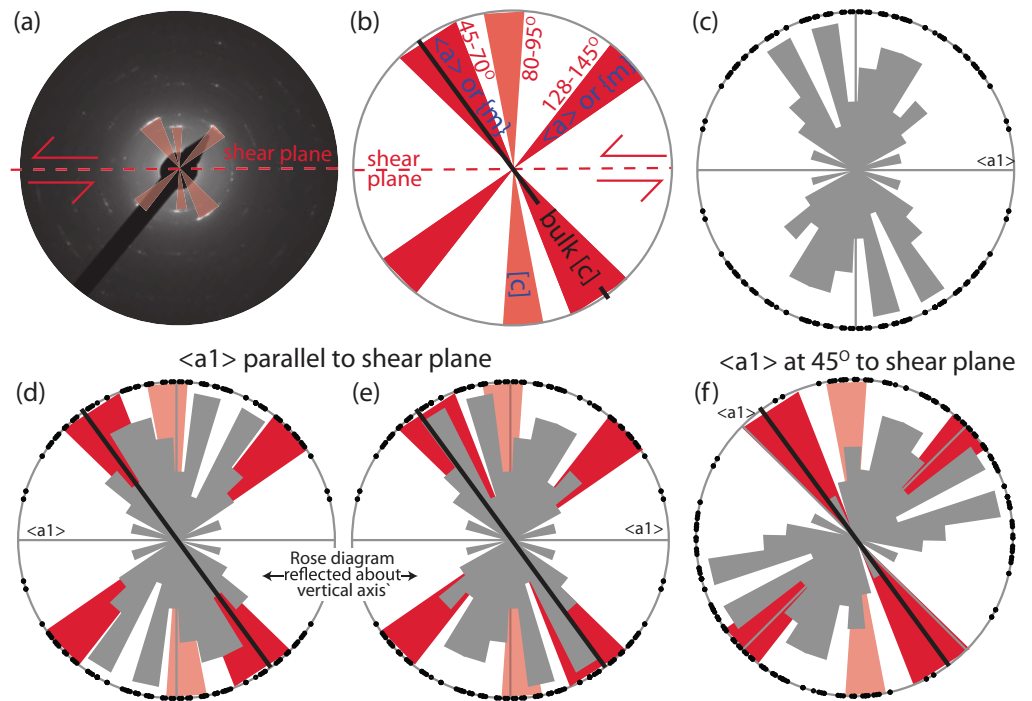


Figure C1. (a) TEM diffraction pattern from partially sintered nanopowder (part of Figure 5e); preferred axis alignments are highlighted in Figure C1b. A rose diagram demonstrating the possible angles between $\langle a \rangle$ if the crystal structure is rotated across favored CSL is presented in Figure C1c. This rose diagram is overlain on the preferred axis alignment plot in Figures C1d–C1f; note that in Figures C1d and C1e, we have reflected the rose diagram about a vertical axis as we are not aware of any way to constrain whether these twins should form by rotation synthetic or antithetic to the shear sense; in Figure C1f, the rose diagram was rotated to 45° to the SZB; reflection about the “NE-SW-striking” plane is also feasible.

- τ_f average shear resistance (Pa);
- \bar{u} average slip (m);
- ρ_{rock} density of the host rock (kg m^{-3});
- c_p specific heat capacity of host rock ($\text{J kg}^{-1} \text{ }^\circ\text{C}^{-1}$);
- ΔT temperature difference between host rock and melt ($^\circ\text{C}$);
- Δh_{fus} latent heat of fusion (J kg^{-1});
- ϕ proportion of unmelted clasts.

For experiment RUB-1, realistic values of these variables are $\tau_f = \Delta\sigma_{max}/2 = 0.42 \text{ GPa}/2 = 0.28 \text{ GPa}$, $\rho_{rock} = 2650 \text{ kg m}^{-3}$, $c_p = 1200 \text{ J kg}^{-1} \text{ }^\circ\text{C}^{-1}$, $\Delta T = (1200-450)^\circ\text{C} = 750^\circ\text{C}$, $\Delta h_{fus} = 5 \times 10^5 \text{ J kg}^{-1}$, and $\phi = 0.3$. when $\bar{u} = 100 \text{ } \mu\text{m}$ (an increment that may have been experienced during a stick-slip event), $t_m = 8.5 \text{ } \mu\text{s}$ (2 s.f.). when $\bar{u} = 700 \text{ } \mu\text{m}$ (i.e., the full displacement in the experiment), $t_m = 73 \text{ } \mu\text{s}$ (2 s.f.).

Table C1. Angular Relationship of [c] to the Shear Plane if Crystallographically Systematic Surfaces Align During Shear

Crystallographic Plane Forming Surface	Angle Between [c] and Shear Plane ($^\circ$)	
	(0001) Parallel Shear Plane	(0001) at 45° to Shear Plane
(0001)	90	45
m{10-10}	0	45
r,z{10-11}	47.7	92.7

Appendix C: Angular Relationships of Crystallographic Axes to the Shear Plane

The most favored CSL, i.e., those that maximize the fraction of coincident lattice points, in order of preference are the Breithaupt twin, which is a 48.9° rotation of (-2111) about $\langle a1 \rangle$; the Sardinian twin, which is a 115.12° rotation of $(0-112)$ about $\{m1\}$; the Cornish twin, which is a 42.97° rotation of $(0-221)$ about $\{m1\}$; a nontwin plane which is associated with

a boundary $(-23-10)$ across which all $\langle a \rangle$ are rotated 21.79° about $[c]$; and the Japan twin, which is an 84.55° rotation of (-2112) about $\langle a1 \rangle$. CSL with these crystallographic relationships will result in angular misorientations of $[c]$ of 48.9° , 115.12° , 42.97° , 0° , and 84.55° , respectively. The twin-plane CSL will result in angular misorientations of $\langle a2 \rangle$ and $\langle a3 \rangle$ of 48.9° , -115.12° , 42.97° , and the nontwin CSL will result in angular misorientations of all three $\langle a \rangle$ of 21.79° . Rotation of the quartz crystal structure according to these relationships yields 112 possible angles between $\langle a \rangle$ axes, which were used to construct the rose diagrams demonstrated in Figures C1c–C1f.

Acknowledgments

We sincerely thank Jörg Renner for scientific input and use of laboratory facilities at Ruhr-Universität Bochum, Agnes Matysiak for help with initial microstructural characterization, Frank Bettenstedt, Brent Pooley, Anja Schreiber, and Sabine Schremmer for sample preparation, Ake Fagereng, Steven Smith, and Luiz Morales for sage advice on early drafts, and two unnamed reviewers for comments on the submission that stimulated us to examine our evidence and discussion more rigorously. Thorsten Becker's patient editorial management is sincerely appreciated. The research was funded by RSNZ Marsden grant UOO0919, the RSNZ International Mobility Fund grant IMF-10-A87, and DAAD award A/10/12522 to V. Toy. Mitchell acknowledges funding by the German Science Foundation (SFB 526) to Jörg Renner and from NERC grant: NE/M004716/1. Data used to construct Figure 1 can be obtained by contacting the first author (virginia.toy@otago.ac.nz).

References

Beeler, N. M., D. A. Lockner, B. D. Kilgore, and D. E. Moore (2011), The transition from frictional sliding to shear melting in laboratory experiments and the implications for scale dependent earthquake source properties, Abstract T54A-01 presented at 2011 Fall Meeting, AGU, San Francisco, Calif., 5–9 Dec.

Bestmann, M., G. Pennacchioni, G. Frank, M. Göken, and H. de Wall (2011), Pseudotachylyte in muscovite-bearing quartzite: Coseismic friction-induced melting and plastic deformation of quartz, *J. Struct. Geol.*, *33*, 169–186.

Bestmann, M., G. Pennacchioni, S. Nielsen, M. Göken, and H. de Wall (2012), Deformation and ultrafine dynamic recrystallization of quartz in pseudotachylyte-bearing brittle faults: A matter of a few seconds, *J. Struct. Geol.*, *38*, 21–38.

Blenkinsop, T. G. (2000), *Deformation microstructures and mechanisms in minerals and rocks*, 150 pp., Kluwer Acad. Publ., N. Y.

Borg, I. (1956), Note on twinning and pseudo-twinning in detrital quartz grains, *Am. Mineral.*, *41*, 792–796.

Boullier, A.-M., T. Ohtani, K. Fujimoto, H. Ito, and M. Dubois (2001), Fluid inclusions in pseudotachylytes from the Nojima fault, Japan, *J. Geophys. Res.*, *106*(B10), 21,965–21,977.

Carter, N. (1976), Steady state flow of rocks, *Rev. Geophys.*, *14*(3), 301–360.

Chan, S., and R. Balluffi (1985), Study of energy vs misorientation for grain boundaries in gold by crystallite rotation method—I. [001] twist boundaries, *Acta Metall.*, *33*(6), 1113–1119.

Chaudhari, P., and J. H. Matthews (1971), Coincidence twist boundaries between crystalline smoke particles, *J. Appl. Phys.*, *42*, 3063–3066.

Chen, X., A. S. Madden, B. R. Bickmore, and Z. Reches (2013), Dynamic weakening by nanoscale smoothing during high-velocity fault slip, *Geology*, *41*(7), 739–742, doi:10.1130/G34169.

Cowan, D. (1999), Do faults preserve a record of seismic slip: A field geologist's opinion, *J. Struct. Geol.*, *21*(8-9), 995–1001.

De Paola, N. (2013), Frictional sliding vs. plastic flow during earthquake propagation in carbonate rocks, paper presented at the 40th Workshop of the International School of Geophysics on Properties and Processes of Crustal Fault Zones, Ettore Majorana Found. and Cent. for Sci. Cult., Erice, Italy, 18–24 May. [Available at http://istituto.ingv.it/resources/conference-archive/conferences-2013/Fault_Zones_Workshop/ and <http://www.ccsem.infn.it/>]

Den Hartog, S. A. M., and C. J. Spiers (2013), Influence of subduction zone conditions and gouge composition on frictional slip stability of megathrust faults, *Tectonophysics*, *600*, 75–90.

Di Toro, G., D. L. Goldsby, and T. E. Tullis (2004), Friction falls towards zero in quartz rock as slip velocity approaches seismic rates, *Nature*, *427*(6973), 436–439.

Di Toro, G., G. Pennacchioni, and G. Teza (2005), Can pseudotachylytes be used to infer earthquake source parameters? An example of limitations in the study of exhumed faults, *Tectonophysics*, *402*, 3–20.

Druiventak, A., C. A. Treppmann, J. Renner, and K. Hanke (2011), Low-temperature plasticity of olivine during high stress deformation of peridotite at lithospheric conditions—An experimental study, *Earth Planet. Sci. Lett.*, *311*, 199–211.

- Friedman, M., J. M. Logan, and J. A. Rigert (1974), Glass-indurated quartz gouge in sliding friction experiments on sandstone, *Geol. Soc. Am. Bull.*, *85*, 937–942.
- Gleiter, H. (1989), Nanocrystalline materials, *Prog. Mater. Sci.*, *33*, 223–315.
- Gleiter, H. (2000), Nanostructured materials: Basic concepts and microstructure, *Acta Mater.*, *48*(1), 1–29.
- Goldsby, D. L., and T. E. Tullis (2002), Low frictional strength of quartz rocks at subseismic slip rates, *Geophys. Res. Lett.*, *29*(17), 1844, doi:10.1029/2002GL015240.
- Green, H. W., II, F. Shi, K. Bozhilov, G. Xia, and Z. Reches (2015), Phase transformation and nanometric flow cause extreme weakening during fault slip, *Nat. Geosci.*, *8*, 484–489, doi:10.1038/ngeo2436.
- Griggs, D. (1967), Hydrolytic weakening of quartz and other silicates, *Geophys. J. R. Astron. Soc.*, *14*, 19–31.
- Hall, A. (Ed.) (1996), *Igneous Petrology*, 2nd ed., Prentice Hall, Essex, U. K.
- Han, R., T. Hirose, T. Shimamoto, Y. Lee, and J. Ando (2011), Granular nanoparticles lubricate faults during seismic slip, *Geology*, *39*, 599–602, doi:10.1130/G31842.1.
- Haynes, W. M. (Ed) (2014), *CRC Handbook of Chemistry and Physics*, 94th ed., CRC Press, Boca Raton, Fla. [Available at <http://www.hbcpnetbase.com/>]
- Hearmon, R. F. S. (1956), The elastic constants of anisotropic materials II, *Adv. Phys.*, *5*, 323–382.
- Heilbronner, R., and J. Tullis (2006), Evolution of c axis pole figures and grain size during dynamic recrystallization: Results from experimentally sheared quartzite, *J. Geophys. Res.*, *111*, B10202, doi:10.1029/2005JB004194.
- Hsu, S. M., J. Zhang, and Z. Yin (2002), The nature and origin of tribochemistry, *Tribol. Lett.*, *13*(2), 131–139.
- Ikari, M., A. Niemeijer, and C. Marone (2011), The role of fault zone fabric and lithification state on frictional strength, constitutive behavior, and deformation microstructure, *J. Geophys. Res.*, *116*, B08404, doi:10.1029/2011JB008264.
- Iler, R. K. (1979), *The Chemistry of Silica: Solubility, Polymerization, Colloid and Surface Properties, and Biochemistry*, John Wiley, N. Y.
- Keller, W., C. Stone, and A. Hoersch (1985), Textures of Paleozoic chert and novaculite in the Ouachita mountains of Arkansas and Oklahoma and their geological significance, *Geol. Soc. Am. Bull.*, *96*(11), 1353–1363.
- Kendall, K. (1978), The impossibility of comminuting small particles by compression, *Nature*, *272*, 710–711.
- Keulen, N., H. Stünitz, and R. Heilbronner (2008), Healing microstructures of experimental and natural fault gouge, *J. Geophys. Res.*, *113*, B06205, doi:10.1029/2007JB005039.
- Kim, J.-W., J.-H. Ree, R. Han, and T. Shimamoto (2010), Experimental evidence for the simultaneous formation of mylonite and pseudotachylite in the brittle regime, *Geology*, *38*(12), 1143–1146.
- Kirkpatrick, J., C. Rowe, J. C. White, and E. E. Brodsky (2013), Silica gel formation during fault slip: Evidence from the rock record, *Geology*, *41*(9), 1015–1019, doi:10.1130/G34483.1.
- Koizumi, Y., K. Otsuki, A. Takeuchi, and H. Nagahama (2004), Frictional melting can terminate seismic slips: Experimental results of stick-slips, *Geophys. Res. Lett.*, *31*, L21605, doi:10.1029/2004GL020642.
- Kronberg, M. L., and F. H. Wilson (1949), Secondary recrystallization in copper, *Trans. Am. Inst. Min. Metall. Pet. Eng.*, *185*, 501–514.
- Law, R. D. (1990), Crystallographic fabrics: A selective review of their applications to research in structural geology, *Geol. Soc. Spec. Publ.*, *54*, 335–352.
- Lee, T.-C., and P. T. Delaney (1987), Frictional heating and pore pressure rise due to a fault slip, *Geophys. J. R. Astron. Soc.*, *88*, 569–591.
- McLaren, A. C. (1986), Some speculations on the nature of high angle grain boundaries in quartz rocks, in *Mineral and Rock Deformation: Laboratory Studies: The Paterson Volume*, pp. 233–245, AGU, Washington, D. C.
- Mykura, H., P. S. Bansal, and M. H. Lewis (1980), Coincidence-site-lattice relations for MgO-CdO interfaces, *Philos. Mag. A*, *42*, 225–233.
- Niemeijer, A. R., and C. J. Spiers (2005), Influence of phyllosilicates on fault strength in the brittle-ductile transition: Insights from rock analogue experiments, *Geol. Soc. Spec. Publ.*, *245*, 303–327.
- Niemeijer, A. R., and C. J. Spiers (2006), Velocity dependence of strength and healing behaviour in simulated phyllosilicate-bearing fault gouge, *Tectonophysics*, *427*(1–4), 231–253.
- Passchier, C. W. (1997), The fabric attractor, *J. Struct. Geol.*, *19*(1), 113–127.
- Pec, M., H. Stünitz, R. Heilbronner, M. Drury, and C. di Capitani (2012), Origin of pseudotachylites in slow creep experiments, *Earth Planet. Sci. Lett.*, *355–356*, 299–310.
- Prior, D. J., R. J. Knipe, R. J. Knipe, and M. R. Handy (1990), Estimates of rates of microstructural changes in mylonites, *Geol. Soc. Spec. Publ.*, *54*, 309–320.
- Ramsay, J. G. (1980), Shear zone geometry: A review, *J. Struct. Geol.*, *2*(1/2), 83–99.
- Reches, Z., and D. Lockner (2010), Fault weakening and earthquake instability by powder lubrication, *Nature*, *467*, 452–455, doi:10.1038/nature09348.
- Rowe, C. D., F. Meneghini, and J. C. Moore (2011), Textural record of the seismic cycle: Strain rate variation in an ancient subduction thrust, *Geol. Soc. Spec. Publ.*, *359*, 77–95.
- Rybacki, E., J. Renner, K. Konrad, W. Harbott, F. Rummel, and B. Stöckhert (1998), A servohydraulically-controlled deformation apparatus for rock deformation under conditions of ultra-high pressure metamorphism, *Pure Appl. Geophys.*, *152*(3), 579–606.
- Schmid, S. M., and M. Casey (1986), Complete fabric analysis of some commonly observed quartz c-axis patterns, in *Mineral and Rock Deformation: Laboratory Studies: The Paterson Volume*, *Geophys. Monogr. Ser.*, vol. 36, pp. 263–286, AGU, Washington, D. C.
- Schubnel, A., F. Brunet, N. Hilaret, J. Casc, Y. Wang, and H. W. Green II (2013), Deep-focus earthquake analogues recorded at high pressure and temperature in the laboratory, *Science*, *341*, 1377–1380.
- Shelly, D. (1971), Hypothesis to explain the preferred orientations of quartz and calcite produced during syntectonic recrystallisation, *Geol. Soc. Am. Bull.*, *82*, 1943–1954.
- Sibson, R. H. (1983), Continental fault structure and the shallow earthquake source, *J. Geol. Soc. London*, *140*, 741–767.
- Sibson, R., and V. G. Toy (2006), The habitat of fault-generated pseudotachylite: Presence vs. absence of friction melt, in *Earthquakes: Radiated Energy and the Physics of Faulting*, *Geophys. Monogr. Ser.*, vol. 170, pp. 153–166, AGU, Washington, D. C.
- Simpson, C., and D. G. De Paor (1993), Strain and kinematic analysis in general shear zones, *J. Struct. Geol.*, *15*, 1–20.
- Smith, S. A. F., G. Di Toro, S. Kim, J.-H. Ree, S. Nielsen, A. Billi, and R. Spiess (2013), Coseismic recrystallization during shallow earthquake slip, *Geology*, *41*, 63–66, doi:10.1130/G3388.1.
- Stünitz, H., N. Keulen, T. Hirose, and R. Heilbronner (2010), Grain size distribution and microstructures of experimentally sheared granitoid gouge at coseismic slip rates—Criteria to distinguish seismic and aseismic faults?, *J. Struct. Geol.*, *32*(1), 59–69, doi:10.1016/j.jsg.2009.08.002.
- Stüwe, K. (2002), *Geodynamics of the Lithosphere*, Springer, Berlin.
- Sundberg, M., and R. Cooper (2008), Crystallographic preferred orientation produced by diffusional creep of harzburgite: Effects of chemical interactions among phases during plastic flow, *J. Geophys. Res.*, *113*, B12208, doi:10.1029/2008JB005618.

- Trimby, P. W. (2012), Orientation mapping of nanostructured materials using transmission Kikuchi diffraction in the scanning electron microscope, *Ultramicroscopy*, *120*, 16–24.
- Trepmann, C. A. (2008), Shock effects in quartz: Compression versus shear deformation—An example from the Rochechouart impact structure, France, *Earth Planet. Sci. Lett.*, *267*(1-2), 322–332.
- Tullis, J., J. M. Christie, and D. T. Griggs (1973), Microstructures and preferred orientations of experimentally deformed quartzites, *Geol. Soc. Am. Bull.*, *84*, 297–314.
- Umemoto, M. (2003), Nanocrystallization of steels by severe plastic deformation, *Mater. Trans.*, *44*, 1900–1911.
- Verberne, B., J. De Bresser, A. R. Niemeijer, C. J. Spiers, D. De Winter, and O. Plümper (2013), Nanocrystalline slip zones in calcite fault gouge show intense crystallographic preferred orientation: Crystal plasticity at sub-seismic slip rates at 18–150°C, *Geology*, *41*(8), 863–866.
- Verberne, B., C. J. Spiers, A. R. Niemeijer, J. De Bresser, D. Winter, and O. Plümper (2014), Frictional properties and microstructure of calcite-rich fault gouges sheared at sub-seismic sliding velocities, *Pure Appl. Geophys.*, *171*, 2617–2640, doi:10.1007/s00024-013-0760-0.
- Verberne, B. J., O. Plümper, D. A. Matthijs de Winter, and C. J. Spiers (2014), Superplastic nanofibrous slip zones control seismogenic fault friction, *Science*, *346*, 1342–1344.
- Wirth, R. (2004), Focused Ion Beam (FIB): A novel technology for advanced application of micro- and nanoanalysis in geosciences and applied mineralogy, *Eur. J. Mineral.*, *16*, 863–876.
- Yang, D. K., P. Cizek, P. D. Hodgson, and C. E. Wen (2010), Microstructure evolution and nanograin formation during shear localization in cold-rolled titanium, *Acta Mater.*, *58*, 4536–4548.